Self-Assembled Monolayers

Monitoring Solid-Phase Reactions in Self-Assembled Monolayers by Surface-Enhanced Raman Spectroscopy

Dominik Scherrer, David Vogel, Ute Drechsler, Antonis Olziersky, Christof Sparr, Marcel Mayor,* and Emanuel Lörtscher*

Abstract: Nanopatterned surfaces enhance incident electromagnetic radiation and thereby enable the detection and characterization of self-assembled monolayers (SAMs), for instance in surface-enhanced Raman spectroscopy (SERS). Herein, Au nanohole arrays, developed and characterized as SERS substrates, are exemplarily used for monitoring a solid-phase deprotection and a subsequent copper(I)-catalyzed azide–alkyne cycloaddition "click" reaction, performed directly on the corresponding SAMs. The SERS substrate was found to be highly reliable in terms of signal reproducibility and chemical stability. Furthermore, the intermediates and the product of the solid-phase synthesis were identified by SERS. The spectra of the immobilized compounds showed minor differences compared to spectra of the microcrystalline solids. With its uniform SERS signals and the high chemical stability, the platform paves the way for monitoring molecular manipulations in surface functionalization applications.

Introduction

The functionalization of solid surfaces with self-assembled monolayers (SAMs) is a widely applied method for surface modifications with applications in catalysis,[1–3] chemical and biochemical sensing,[4–6] molecular electronics,[7–9] wettability,[10] corrosion prevention,[11] and many others. Various functionalization methods rely on a stepwise assembly or a modification of the SAMs.[12] Due to the differences in the chemical and physical behavior of molecules attached to surfaces compared to their crystalline or liquid form, the composition of these molecular layers is ideally characterized upon each assembly and modification step. For such purposes, however, only a few surface analytical methods exist that provide a high enough sensitivity to determine the elemental composition (X-ray photoelectron spectroscopy), the topology (scanning tunneling microscopy, atomic force microscopy), the lattice structure (near-edge X-ray absorption fine structure spectroscopy), the surface layer thickness (ellipsometry), or the surface coverage (thermal gravimetric analysis and electrochemical methods).[13–16] While these methods provide the above-mentioned information about a surface, many of them lack the ability to characterize the chemical composition of a surface, e.g., to detect functional groups within the SAM. In that respect, infrared (IR) spectroscopy and variants thereof including Fourier-transform IR (FTIR) spectroscopy, polarization-modulation infrared reflection–absorption spectroscopy (PM-IRRAS) are sensitive enough to measure solid thin films to provide information about the chemical functional groups present in a SAM.[17–20] Raman spectroscopy is an optical characterization method that relies on inelastic scattering of incident, monochromatic light at chemical bonds. It can therefore provide substantial information about the chemical composition of the specimen,[21] at least for Raman-active bonds. Contrary to IR spectroscopy, where bonds with large dipole moments exhibit the highest signal intensities, bonds that are non-polar and polarizable are generally highly Raman-active. IR and Raman spectroscopy are therefore used mostly complementary, as (with exceptions) many IR-inactive (or weakly active) molecular vibrations are Raman-active and vice versa. An advantage of Raman over IR spectroscopy is that it can be used in aqueous solutions as well, while IR suffers from the strong IR self-absorption of H_2O which may mask other bonds of interest.[22] In return, Raman spectroscopy is a second-order and therefore an inherently weak process (with Raman scattering probabilities of 10^{-14} to 10^{-7}, and cross-sections of 10^{-30} to 10^{-25} cm^2 for a single molecule). This is usually compensated for by probing multiple thousands of molecules in parallel to obtain an adequate signal intensity, using high laser intensities or long acquisition times. Another method to increase Raman signal intensities is to locally concentrate incident electromagnetic radiation, E_{local},

[*] D. Scherrer, U. Drechsler, Dr. A. Olziersky, Dr. E. Lörtscher
Science and Technology Department, IBM Research Europe
Säumerstrasse 4, 8803 Rüschlikon (Switzerland)
E-mail: eml@zurich.ibm.ch

D. Scherrer, D. Vogel, Prof. C. Sparr, Prof. M. Mayor
Department of Chemistry, University of Basel
St. Johanns-Ring 19, 4056 Basel (Switzerland)
E-mail: marcel.mayor@unibas.ch

Prof. M. Mayor
Institute for Nanotechnology (INT)
Karlsruhe Institute of Technology (KIT)
P. O. Box 3640, 76021 Karlsruhe (Germany)
and
Lehn Institute of Functional Materials (LIFM)
School of Chemistry, Sun Yat-Sen University (SYSU)
Guangzhou 510275 (P.R. China)
E-mail: marcel.mayor@kit.edu

by employing field-enhancing near-field methods, for example, surface plasmon polaritons. These methods are generally referred to as surface-enhanced or tip-enhanced Raman spectroscopy (SERS and TERS, respectively) with many variants. Their corresponding Raman scattering intensities, I_{Raman}, roughly scale with $|E_{local}|^4$ (at least close to the near-field surface).[23–30] SERS and TERS thereby enable ambient and label-free analytics of the molecule's unique vibrational fingerprint. While TERS relies primarily on coating a scanning microscopy tip with an appropriate material and bringing it in close proximity with the specimen, various SERS methods and substrates have been developed (usually containing plasmonically active materials such as Cu, Ag, or Au): On the one hand, SERS substrates, such as bottom-up self-assembled Au nanospheres[31] and top-down fabricated nano-gaps[23] or black Si-based nanoforests,[32] can deliver exceptionally high field enhancements (FEs). But on the other hand, it is difficult to control the nanoscale hotspots as they are usually non-uniformly distributed on the surface and found to be sensitive to irradiation, temperature, or chemical environments. Consequently, these substrates cannot be treated by single-spot measurements alone but require time-consuming surface mappings to locate the hotspots. Top-down substrates, which are micro- and nanopatterned using lithography, are compatible with mass-production manufacturing.[23,24,29,33,34] They usually provide smaller field enhancements than the nano-gaps of bottom-up assembled particles but are easier to control and more uniform. Furthermore, they enable a deterministic and reliable integration into more complex device architectures, for example, in microfluidic systems or gas and liquid sensing devices.[36] Over the last years, SERS has evolved from an exploratory research topic to an established analytical tool with fully characterized SERS substrates and various applications, for example, in microplate readers in medicine and biology. In contrast, rather than tracking indirect shifts in the plasmon resonance of the SERS substrate as is commonly done, we employ the substrate's field enhancements for SERS to characterize SAMs that provide too small Raman signals on unpatterned surfaces. Moreover, we use these substrates to monitor solid-phase reactions, specifically a copper(I)-catalyzed azide–alkyne cycloaddition (CuAAC) "click" reaction[37,38] and describe species-specific vibrational modes by tracking their evolution for various molecular model systems upon chemical modification.

Results and Discussion

For SERS-based chemical structure determination and the monitoring of chemical reactions that occur in surface-bound molecules, one requirement is a surface patterning that yields quantitatively reproducible and homogeneously distributed field-enhanced areas rather than a few high SERS-intensity hotspots that are not representative of the entire SAM. To meet these requirements, plasmonic nanohole arrays with a moderate FE were chosen as a platform. In return, they probe a comparably large number of molecules across the whole area of interest.[33] A poly(methyl meth-acrylate) (PMMA)/hydrogen silsesquioxane (HSQ) two-layer electron-beam lithography (EBL) lift-off process was developed (see SI) to fabricate such nanohole arrays (10×10 µm² in size each) with quantitative lift-off yield in a 30 nm thick Au thin film on a monocrystalline Si substrate. By scanning electron microscopy (SEM), the arrays were found to be defect-free and reveal homogeneous shapes and thicknesses (Figure 1 A,B). A variety of diameters and pitches were tested to optimize the nanohole array for two excitation laser wavelengths (633 nm and 785 nm) by empirically screening the geometrical parameter space with a 4-nitrothiophenol (4-NTP) SAM as a reporter compound. Arene-thiols were chosen as they are known to form stable SAMs on Au surfaces.[17] The nanohole array dimensions that showed the highest plasmonic Au fluorescence and SERS signals were a 180 nm hole diameter with a pitch of 225 nm in a cartesian arrangement (elliptical holes were disregarded in the consideration for simplified EBL). The SERS enhancement factor (EF) of the nanohole arrays was determined experimentally (see Supporting Information (SI)) and reached a value of 86 ± 29 (standard error).[39,40] This was confirmed by finite-difference time-domain (FDTD) calculations (Figure 1 C; see SI). To validate the SERS performance and the uniformity of the substrate for the 4-NTP test compound, Raman spectra were recorded under ambient conditions with a liquid N_2 cooled Si-CCD and a 300 grooves mm⁻¹ grating at 633 nm excitation (7.5 mW laser power) with a $100 \times$ objective with 0.86 NA and by using variable neutral density filters. A 633 nm excitation wavelength was chosen even though the maxima of the plasmonic activity of Au would be more in the near-infrared region of the electromagnetic spectrum. However, measurements with 785 nm excitation do not lead to stronger signals (see Figure S3 in the SI)). The confocal Raman microscope has a spot size smaller than 1 µm and a piezo-electric stage enables 3D scanning of entire nanohole arrays with sub-nm spatial accuracy.

Figure 1 D shows a 10×10 single-spot SERS map of a 4-NTP SAM immobilized on a Au nanohole array (gray traces) mapped with a step size of 0.96 µm, covering an area of approx. 75 µm². The solid black trace represents the averaged spectrum and the gray dashed lines represent the peaks of a reference spectrum.[41] All spectra show eight distinct peaks with the most prominent one located at 1327 cm⁻¹, corresponding to the symmetric stretch frequency of NO_2. The intensity varies from approximately 1600 to 3600 counts for the most prominent peak, which is a reasonable range, showing that every single-spot measurement delivers a suitable spectrum (Figure 1 F). The noise in the spectra is approximately 200 counts prior to signal processing. In contrast to measurements on Au nanoholes, a SAM of 4-NTP grown on an unpatterned Au surface under the same conditions does not yield discernible Raman peaks (Figure 1 D, dashed orange trace). Hence, the FE of the nanohole arrays causes Raman signatures of 4-NTP SAMs to appear. In addition to the good quantitative uniformity of the SERS intensity over the entire nanohole array, the corresponding Raman peak positions are also located ± 1.0 cm⁻¹ (fitted values) around the mean peak values, as shown for the three strongest signals in the box plot in Figure 1 E (spectral
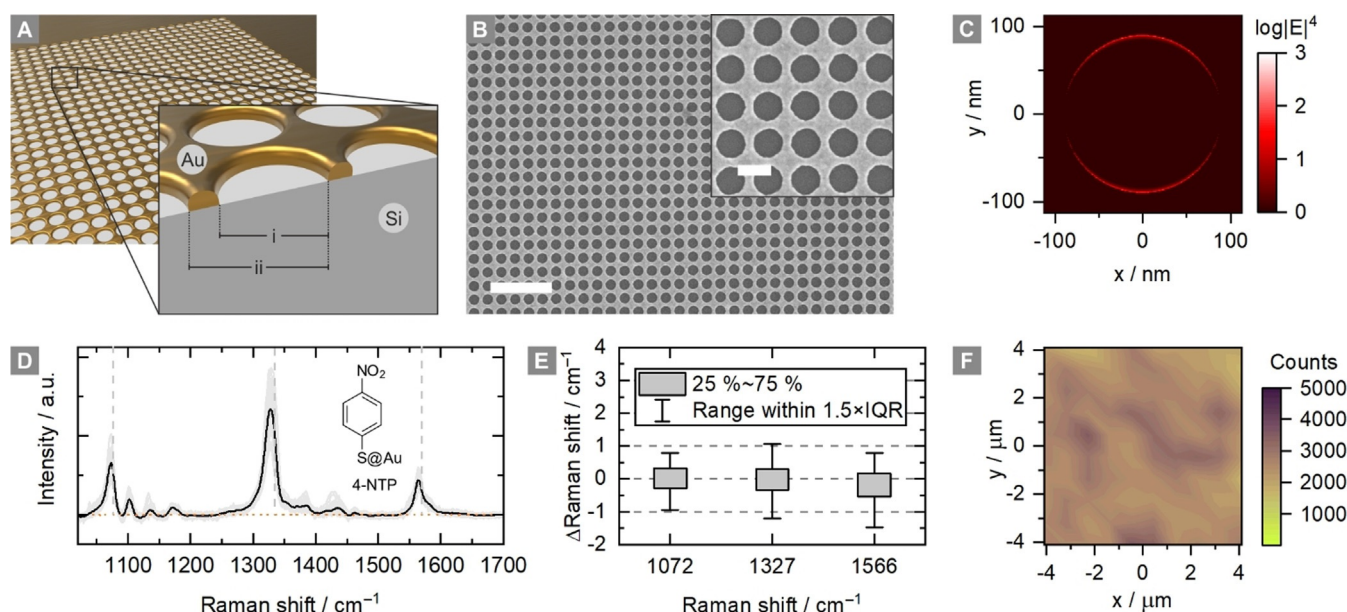
Figure 1. A) Schematic representation of a monocrystalline Si chip with Au nanohole arrays (0.5 nm Cr, 30 nm Au), nanohole dimensions: i = 180 nm, ii = 225 nm; B) scanning electron micrographs of a Au nanohole array (scale bar = 1 μm, insert scale bar = 200 nm). C) Calculated enhancement factor ($|E|^4$) in log scale for a Au nanohole array on Si (x,y plane of the Au–air interface). D) 100 SERS spectra (gray traces) and averaged spectrum (solid black trace) of a 4-nitrothiophenol (4-NTP) SAM on a Au nanohole array, in comparison to the Raman spectrum of 4-NTP on an unstructured, planar Au surface (dashed orange trace). The vertical gray lines indicate the peak positions of a reference spectrum.[35] E) Box plot of the peak position distribution for the three most intense Raman signals of 4-NTP on a Au nanohole array as a deviation from the respective mean peak position. The gray boxes and the whiskers indicate the inner quartile range (IQR) and the range within 1.5×IQR, respectively. F) Heat map of the peak height at 1327 cm^{-1} of 4-NTP on Au nanohole arrays, illustrating the quantitative uniformity of the signal intensity over the entire map measurement.

resolution = 1.8 cm^{-1}). This confirms that the molecular intrinsic modes are only weakly, if at all, disturbed by the covalent coupling of the Raman active moieties to the Au surfaces via thiols. The fact that SERS spectra can be acquired everywhere on the Au nanohole substrate with a high uniformity allows single-spot measurements to be conducted instead of time-consuming mappings to detect suitable hotspots. Consequently, the nanohole arrays serve the purpose of chemically characterizing SAMs by SERS with stable and uniform FEs. Notably, no additional SiO$_X$ adhesion layer on top of the Au was used as a mediating SAM-binding layer, for instance via silanes, or as a stabilizing layer to prevent diffusion of Au surface atoms at elevated temperatures (induced by the incident laser power). Instead, the SAMs are directly grown on Au and immobilized via a Au−S linkage. Finally, all the employed materials (Si, Au, and Cr as adhesion layer between the former two) are chemically inert under the environments of interest. Therefore, these substrates are compatible with monitoring chemical changes in SAMs prior to and after exposing the entire substrate to wet chemical reaction conditions.

As a test system for conducting chemical reactions on the SAMs and to monitor them by SERS, we chose small molecules that have got a low number of Raman active vibrational modes that can be unambiguously assigned to specific chemical bonds. For these compounds, the goal is to exemplarily show the deprotection and a subsequent chemical transformation by SERS. The synthesis and characterization of all compounds are described in the SI. To allow a directed

immobilization on Au surfaces via Au−S linkage, thioacetate **1a** carries two orthogonal protecting groups; an acetyl protecting group on the S terminus and trimethylsilyl (TMS) on the alkyne terminus. The acetyl moiety prevents oxidative S−S bond formation, while TMS prevents bonding of the alkyne to Au (Figure 2). This design allows an asymmetric, controlled cleavage of the S-acetyl to form the Au−S linkage, causing the alkyne to point upwards from the Au surface because it is still TMS-protected. This configuration provides both an immobilization on Au and a susceptibility to subsequent chemical modifications. Thioacetate **1a** was immobilized as a SAM on the Au nanohole arrays by immersing a sample in a 5 mM ethanolic solution of **1a** with an excess of NH$_3$ (to deprotect the thiol) for 24 h (step (a) in Figure 2). After functionalization, the chip was immersed in H$_2$O and EtOH baths accompanied by ultrasonication to remove physisorbed **1a** as well as byproducts from the acetyl deprotection and impurities. Optical inspection under the microscope was performed to rule out the presence of visible aggregates and particles. Subsequently, single spot SERS spectra were recorded under ambient conditions and using a 633 nm excitation source. A SERS spectrum of the TMS-protected monolayer (**1b**) is depicted in Figure 2 (red). The most prominent Raman signals (full range spectra in Figure S19 in the SI) include the signals at 1072 cm^{-1}, 1176 cm^{-1}, and 1581 cm^{-1} that can be assigned to vibrational modes of the substituted benzene. The peak at 2155 cm^{-1} corresponds to the symmetric C≡C stretch frequency of the TMS-protected alkyne.[22,42] The spectrum of the SAM of **1b** is
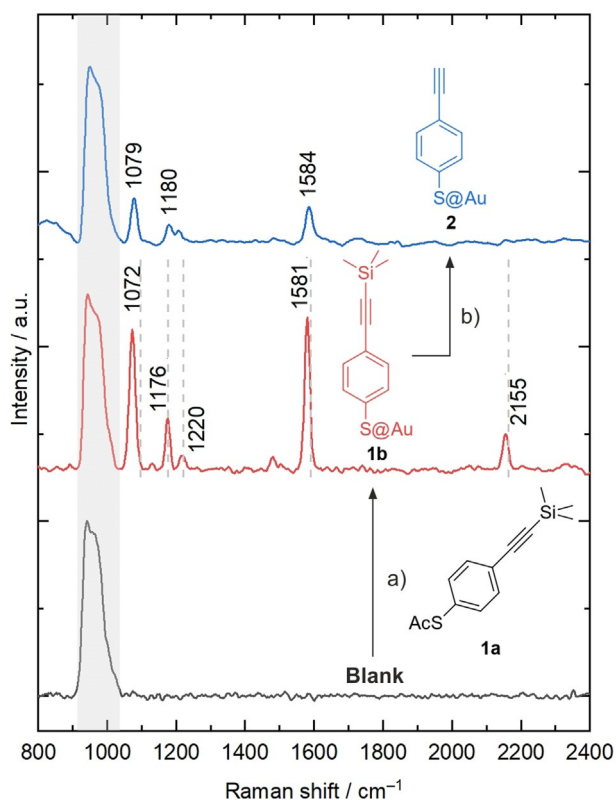
Figure 2. Immobilization of **1a** on a Au nanohole array and subsequent trimethylsilyl (TMS) deprotection: SERS spectra of a blank Au nanohole array (black), TMS-protected alkyne (**1b**, red), and deprotected alkyne (**2**, blue) SAMs on a Au nanohole array at 633 nm excitation. The Si signal of the substrate (2nd order LO) is marked with a gray bar. The values above the signals denote the respective Raman shift in cm^{-1}. The spectra were separated for better visibility. The vertical dashed gray lines indicate the peak positions of the Raman spectrum of the corresponding solid. Reagents and conditions: a) Au nanohole array chip, **1a**, NH$_3$ (7 M in MeOH), EtOH, 23 °C, 24 h; b) tetrabutylammonium fluoride (TBAF), tetrahydrofurane (THF), ultrasound, 40 °C, 1 h.

closely comparable to the Raman spectrum of its bulk analogue (**1a**) in crystalline form (gray dashed lines; see Figure S17 in the SI for the full spectra). The small spectral shifts observable between the SERS spectrum of the immobilized molecule and to the one of its crystalline state can be attributed to the change in the substitution at the aromatic ring (-SAc vs.-S@Au) and to the different intermolecular forces the molecule experiences in a solid compared to a SAM.

As indicator for chemical modifications of the SAM of **1b**, alterations in the corresponding SERS spectrum, ranging from shifts in the peak positions to disappearances or appearances of peaks, were used as discriminating features after each step. This monitoring only takes a few minutes and can be done non-destructively, non-invasively, and contact-free. At the same time, it is still highly sensitive for the detection of changes in the chemical structure. After the SAM formation, the alkyne was deprotected by releasing the TMS protecting group to enable a CuAAC reaction on the terminal alkyne. TMS deprotection with K$_2$CO$_3$ was found to be

unsuccessful, as no change in the Raman signals occurred. However, deprotection with TBAF in an ultrasonic bath led to the disappearance of the signal at 2155 cm^{-1} as shown in Figure 2 (blue). A notable difference was observed between the expected and the measured changes in the Raman spectrum after TMS deprotection; the symmetric C≡C signal is expected to have a vibrational frequency between 2130 and 2100 cm^{-1},[22, 42] which is a slightly lower frequency range than the one for the TMS-protected alkyne (2155 cm^{-1}). Surprisingly, no signal for the alkyne was detected after the deprotection. These results underline the importance of evaluating the unique characteristics of Raman-active vibrations of immobilized molecules on plasmonic surfaces.

After detecting a change in the spectra before and after the TMS deprotection for an immersion time of 1 h, it was particularly interesting to investigate whether the decay of the signal at 2155 cm^{-1} during the conversion from **1b** to **2** could be monitored over time by measuring several spectra after short reaction intervals. Under homogeneous conditions, this reaction would be expected to complete within just a few seconds. This was confirmed by deprotecting the precursor **1a** in a homogeneous solution with TBAF. NMR analysis showed the deprotection to be finished within less than 1 min (see Figure S21B in the SI). Contrary to the reaction in solution, the TMS deprotection of SAM **1b** was expected to proceed at a lower rate (potentially within minutes instead of seconds) because of the steric hindrance the TMS group experiences due to the neighboring immobilized molecules of the SAM, as well as reduced mass-flow exchange at the surface. The deprotection of the TMS group of **1b** was therefore studied by repetitively removing the chip from the TBAF solution in THF at specific intervals to wash and dry it and subsequently measure the SERS of the SAM. Figure 3 A shows the SERS signal of the pristine (as-grown) **1b** SAM on the Au nanohole array right after its formation (0 min; red trace), after 1 min (dark red trace), 5 min (violet trace), as well as 10 min (blue trace) of immersion in the TBAF solution in THF. Each spectrum is the average of three individual point spectra that were recorded at three randomly chosen points on the nanohole array. The signal strength of the disubstituted alkyne peak (symmetric C≡C stretch frequency) at approximately 2155 cm^{-1} decreases after 1 min as well as after 5 min, but it is still visible (Figure 3 A, inset). The measurement after 10 min of immersion, however, does not reveal a signal that can be distinguished from the baseline anymore. This suggests that the TMS deprotection of a **1b** SAM is completed after 10 min while a partial conversion of the **1b** SAM towards a full **2** SAM could be monitored in time. The spectra in Figure 3 A (like all herein presented spectra) have been smoothed and baseline-subtracted. The non-treated data show the same result and can be consulted in the SI (Figure S21A). The development of the intensity of the three signals in Figure 3 A that are marked with a gray, dashed line and have a square, circle, or triangle as a label is plotted over time in Figure 3 C. The error bars indicate the standard deviation from three randomly chosen point measurements on the surface, in agreement with the fluctuation in Figure 2 and typical for SERS. Despite these fluctuations, it can be concluded from Figure 3 C that the signal at 2155 cm^{-1}
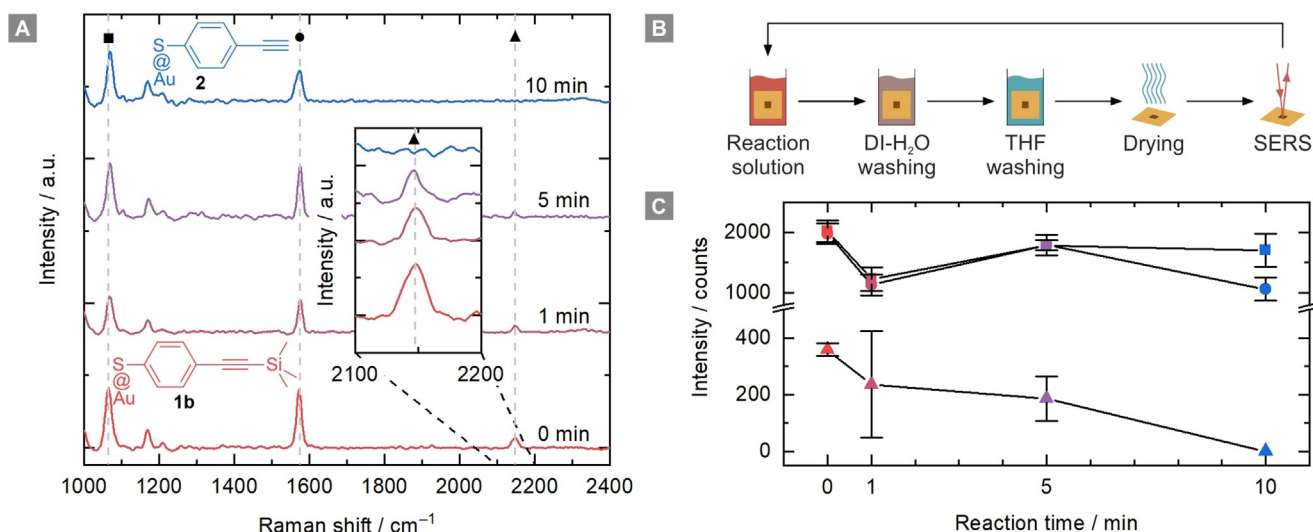
Figure 3. A) SERS spectra taken after different reaction times (0 min, 1 min, 5 min, 10 min) during TMS deprotection of a **1b** SAM (red) forming a **2** SAM (blue) with TBAF (50 mm) in THF, followed by washing in DI-H_2O and THF and drying (633 nm excitation; non-treated data in Figure S21A in the SI). Each spectrum is the average of three spectra that were recorded at different, randomly chosen points on the nanohole array. The inset shows a zoom on the symmetric C≡C stretch frequency located at 2155 cm^{-1} which vanished after 10 min. B) Illustration of the repeated sequence of immersing the sample in the reaction solution, washing, drying, followed by spectra acquisition. C) Development of the peak intensities of the three signals that are labeled with a square, a circle, and a triangle in (A) over the course of 10 min total reaction time. The peak intensities in counts were determined by fitting the respective peaks (Gaussian fit) of three spectra recorded at different, randomly chosen points on the nanohole array. The error bars indicate the standard deviation of the three measurements. None of the three spectra after 10 min displayed a signal at 2155 cm^{-1} above the measurements noise level (see inset in (A)) and the blue triangle was therefore set to zero and no error bar was added.

(triangle) gradually declines while the other signals remain at a relatively high level. Although quantitative evidence about peak intensities for these measurements is difficult to establish due to the high intensity fluctuations between SERS measurements, the stability of the SAMs **1b** and **2** in ultrasonic conditions was studied to learn whether large quantities of the SAMs dissociate under these conditions by following the signal intensities over time. Figure S22 in the SI shows that prolonged ultrasonic exposure does not cause the signal intensities to fall below the detection limit. To summarize, the above-mentioned time-resolved experiments show that the presented method can not only be used to characterize the SAMs prior to and after a reaction, but also to follow the partial and gradual conversion of molecules inside a SAM in time, at least for slow reactions such as the TMS deprotection on the surface. The stepwise monitoring provides clear evidence that the reaction is taking place at the SAM interface.

Next, we performed a CuAAC reaction to attach 1-azido-4-nitrobenzene (**3**) to the liberated alkyne of **2** (Scheme 1). Working with a SAM-coated surface on Au as reactant requires homogeneous reaction mixtures rather than suspensions, as the presence of precipitates may cause aggregation of particles forming thin films on the surface. These thin films can be difficult to remove without affecting the nanostructures underneath and the SAM itself. Hence, a series of reaction conditions was screened to evaluate a suitable catalyst, as well as other reagents, solvents, and concentrations (see SI). CuSO$_4$·5H$_2$O with sodium ascorbate as
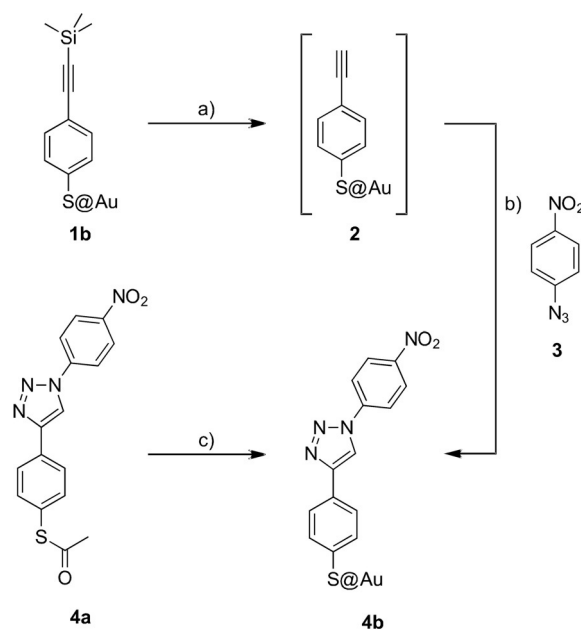
Scheme 1. Deprotection of a) the TMS-protected alkyne of **1b** with b) the immediately following CuAAC reaction on the liberated alkyne of **2** on Au nanohole arrays, yielding triazole **4b**. c) Immobilization of **4a** on Au nanohole arrays. Reagents and conditions: a) TBAF, THF, ultrasound, 40°C, 1 h; b) 1-Azido-4-nitrobenzene (**3**), CuSO$_4$·5H$_2$O, sodium ascorbate, THF/H_2O, ultrasound, 40°C, 1 h, then 23°C, 16 h; c) Au nanohole array chip, NH$_3$ (7 m in MeOH), CHCl$_3$, 23°C, 5.5 h.
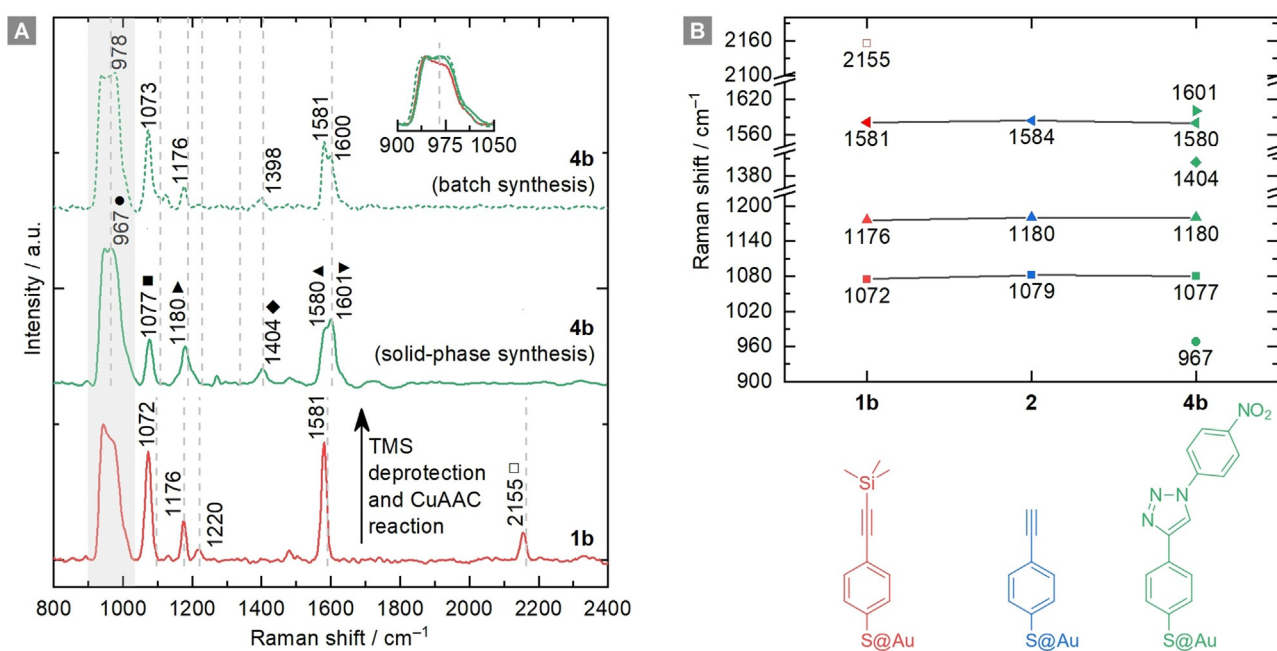
Figure 4. A) SERS spectra of TMS-protected alkyne at (**1b**, red), as well as the triazole originating from the solid-phase synthesis on the SAM (**4b**, solid green) and from the batch synthesis (**4b**, dashed green) at 633 nm excitation. The broad 2nd order LO band of the Si substrate is marked with a gray bar. The values above the signals denote the respective Raman shift in cm^{-1}. The vertical dashed gray lines indicate the peak positions of the Raman spectra of the corresponding solids. B) The appearance, evolution, and disappearance of the individual SERS signals before and after functionalization, upon TMS deprotection, and CuAAC reaction.

reducing agent in THF/H$_2$O with ultrasound at 40°C was found to be a suitable combination to provide the required homogeneous mixture. The SERS spectra prior to and after the coupling of azide **3** onto alkyne **2**, yielding triazole **4b**, are depicted in Figure 4A. When comparing the spectrum of **4b** (solid green) to the spectrum before deprotection and CuAAC reaction (red), the alkyne peak at 2155 cm^{-1} has vanished and three new peaks have appeared: Next to the peak at 1581 cm^{-1} of **1b**, a peak at 1601 cm^{-1} appears with a comparable intensity; the two signals are not baseline-separated. The new peak can be attributed to a vibrational mode of the added benzene ring with a slightly different energy caused by the different substitution of the two rings. At 1404 cm^{-1}, a weaker peak evolves from the baseline that originates from the C—N stretching mode of the triazole.[43] Further, a third new peak located at 967 cm^{-1} can be discerned. It superimposes the broad 2nd order longitudinal optical (LO) band from the Si substrate (Figure 4A, inset). Around 1325 cm^{-1}, however, no peaks appear in the spectra of **4b**. Such signals representing the symmetric stretch frequency of the terminal NO$_2$ of **4b** would be expected after the CuAAC reaction clicking **3** to **2**. The NO$_2$ moiety is known to be Raman active and was also clearly observed in the 4-NTP spectra acquired on Au nanohole arrays, even as the most prominent peak at 1327 cm^{-1} presented in Figure 1D. Figure 4B illustrates the appearance, the evolution, and the disappearance of the individual SERS peaks over the course of all steps of the experiment. While this evolution was deemed reasonable, the disappearance instead of a shift of the peak at 2155 cm^{-1} upon TMS deprotection remains anom-

alous as it clearly corresponds to the symmetric C≡C stretch frequency of the alkyne. Also, the missing NO$_2$ peak, as discussed above, is distinct from existing literature data. In order to confirm that **4b** has indeed been formed by the solid-phase reactions on the SAM, a control experiment was executed through synthesizing **4a** with classic batch synthesis methods (see SI). Batch-synthesis-derived **4a** was immobilized on Au and its SERS spectrum measured (Scheme 1 and Figure 4A, dashed green curve). When comparing it with **4b** produced by solid-phase synthesis (solid green curve), the two spectra are qualitatively almost identical, with some small quantitative deviations in the relative peak intensities of the two benzene vibrations at 1580 cm^{-1} and 1601 cm^{-1}. The peaks at 1077 cm^{-1} and 1180 cm^{-1} are almost equally intense in the solid green curve, but the peak at 1073 cm^{-1} is much more pronounced than the peak at 1176 cm^{-1} in the dashed green curve. More importantly, however, also in the batch-synthesis-derived **4b**, the peaks at 2155 cm^{-1} as well as 1327 cm^{-1} are clearly below the detection limit. When comparing this with bulk Raman spectra of the microcrystalline solids (see Figure S17 of the SI) excited at 785 nm, however, the NO$_2$ signal is present, both in **3** and **4a**. In contrast, bulk measurements at 633 nm provide less informative spectra as they are dominated by a fluorescent background (see Figure S18 in the SI). We therefore tentatively rationalize the absence of the usually Raman active symmetric C≡C stretch frequency of the alkyne moiety of the TMS-deprotected **1b** and the NO$_2$ in the Au-bound **4b** with the very low Raman cross-section due to specific optical scattering geometries on surfaces or quenching of the Raman-scattered

phonon. The overall agreement of the two SERS spectra of the differently derived compounds **4b**, however, leads to the conclusion that the deprotection and CuAAC reaction on the SAM immobilized on Au nanohole substrates can be unequivocally monitored by SERS. Further control experiments were performed to rule out that the reagents of the CuAAC reaction adhere to the Au surface and could be responsible for the change in the spectrum (see Scheme S2 and Figure S20 in the SI). Given the double-checked and confirmed differences in the Raman spectra of immobilized compounds to their bulk counterparts, it becomes apparent that SERS is distinctly suitable for detecting minor features in the chemical structure of SAMs, but its empirical determination is currently still mandatory for SERS-based surface characterizations.

Conclusion

We have shown the possibility of characterizing different intermediates during the chemical modification of a SAM on a structured Au nanohole array. The Au nanohole array acts as a plasmonic surface that provides a uniform FE over the whole patterned area, allowing single-spot SERS measurements. The starting material and the product of the studied solid-phase CuAAC reaction produce distinguishable Raman spectra that match with the spectra of the corresponding batch-synthesized compounds. While the CuAAC reaction serves as a suitable model reaction, a broad range of short-chained SAMs is considered as suitable substrates and analytes for functional surface modification. While most peaks in the SERS spectra can be unambiguously attributed to chemical bond vibrations from data bases, SERS shows unique effects as peaks may disappear on surfaces as shown in this work, motivating the further investigation of this interesting feature. Therefore, it is important to compare the reactions on the surface with their batch-synthesis analogues. Notably, the presented SERS platform enables detailed monitoring of chemical reactions for solid-phase synthesis by providing very fast, contact-free, non-destructive, and non-invasive information about the surface functionalizations and the modifications thereof.

As the nanohole arrays can be created with a variety of plasmonically active materials and only a tiny area needs to be nano-patterned, it is anticipated that such monitoring tags might become useful for process monitoring in a variety of industry-relevant applications. As an example, we foresee this method to be used to miniaturize currently existing systems for reaction screenings in which the chemical substrates are immobilized on solid supports (e.g. on resins). Reaction screenings that aim to find pharmaceutical leads require a vast number of possible candidate substances. Such systems include the combinatorial synthesis of peptides and other biologically active molecules on solid supports.[44] Miniaturization of these systems would mean using a single molecular monolayer on a Au surface instead of the substrate being immobilized on resin beads. The need for less resources with possibly lower required reaction volumes could be an advantage of such a miniaturized system. If plasmonic surfaces are integrated in a microfluidic device and if the synthesized molecules can be released in a controlled manner, it could be linked to other lab-on-a-chip modules such as biological assays to assess the binding to a protein target in an integrated system, for instance. The herein reported method would greatly benefit from further developments to be viable for such an application. Firstly, the FE produced by the presented nanostructures is only strong enough in a certain energy range of the spectrum and does not cover the parts of the spectrum above approximately 2500 cm^{-1}. Complementary plasmonic nanostructure designs are expected to intensify the Raman signals also at higher wavenumbers to detect and monitor C−H, O−H, and N−H vibrations. Secondly, it would be desirable if the samples could be kept in the solution and the chemical transformations of the SAMs could be followed in-line, instead of a separate location. This would enable real-time measurements upon conducting the reactions and thereby avoid interrupting the processes. Thirdly, monitoring a broad variety of chemical reactions and substrates will establish the full capacity of the method. Further improvements on the plasmonic nanohole arrays are currently in development: masking the Si signals originating from the underlying carrier wafer below the Au layer is envisioned to provide fewer background signals that overlap with signals from the SAMs and the integration of nanohole arrays in Au thin-film electrodes as SERS tags will enable performing electrochemical reactions on SAMs. We anticipate that the method presented herein will allow the detection of various reactions at SAMs, enable profound applications for various disciplines and that technical improvements will render high precision assay development feasible.

Conflict of Interest

The authors declare no conflict of interest.

Keywords: click chemistry · field enhancement · Raman spectroscopy · self-assembled monolayers · solid-phase synthesis

[1] G. Zaupa, C. Mora, R. Bonomi, L. J. Prins, P. Scrimin, *Chem. Eur. J.* **2011**, *17*, 4879–4889.

[2] C. A. Schoenbaum, D. K. Schwartz, J. W. Medlin, *Acc. Chem. Res.* **2014**, *47*, 1438–1445.

[3] G. Pieters, L. J. Prins, *New J. Chem.* **2012**, *36*, 1931–1939.

[4] N. K. Chaki, K. Vijayamohanan, *Biosens. Bioelectron.* **2002**, *17*, 1–12.

[5] N. A. S. Omar, Y. W. Fen, J. Abdullah, Y. Mustapha Kamil, W. M. E. M. M. Daniyal, A. R. Sadrolhosseini, M. A. Mahdi, *Sci. Rep.* **2020**, *10*, 2374.

[6] S. Flink, F. C. J. M. van Veggel, D. N. Reinhoudt, *Adv. Mater.* **2000**, *12*, 1315–1328.

[7] P. T. Mathew, F. Fang, *Engineering* **2018**, *4*, 760–771.

[8] G. D. Kong, S. E. Byeon, S. Park, H. Song, S. Kim, H. J. Yoon, *Adv. Electron. Mater.* **2020**, *6*, 1901157.

[9] S. Casalini, C. A. Bortolotti, F. Leonardi, F. Biscarini, *Chem. Soc. Rev.* **2017**, *46*, 40–71.

[10] S. Rittikulsittichai, C. S. Park, A. C. Jamison, D. Rodriguez, O. Zenasni, T. R. Lee, *Langmuir* **2017**, *33*, 4396–4406.

[11] L. Srisombat, A. C. Jamison, T. R. Lee, *Colloids Surf. A* **2011**, *390*, 1–19.

[12] T. P. Sullivan, W. T. S. Huck, *Eur. J. Org. Chem.* **2003**, 17–29.

[13] E. Colangelo, J. Comenge, D. Paramelle, M. Volk, Q. Chen, R. Lévy, *Bioconjugate Chem.* **2017**, *28*, 11–22.

[14] C. Yan, M. Zharnikov, A. Gölzhäuser, M. Grunze, *Langmuir* **2000**, *16*, 6208–6215.

[15] J. Liu, B. Schüpbach, A. Bashir, O. Shekhah, A. Nefedov, M. Kind, A. Terfort, C. Wöll, *Phys. Chem. Chem. Phys.* **2010**, *12*, 4459–4472.

[16] S. Zhang, K. L. Chandra, C. B. Gorman, *J. Am. Chem. Soc.* **2007**, *129*, 4876–4877.

[17] C. Vericat, M. E. Vela, G. Benitez, P. Carro, R. C. Salvarezza, *Chem. Soc. Rev.* **2010**, *39*, 1805–1834.

[18] S. Chakrabarty, S. Maity, D. Yazhini, A. Ghosh, *Langmuir* **2020**, *36*, 11255–11261.

[19] K. Rajalingam, L. Hallmann, T. Strunskus, A. Bashir, C. Wöll, F. Tuczek, *Phys. Chem. Chem. Phys.* **2010**, *12*, 4390.

[20] S. A. Swanson, R. McClain, K. S. Lovejoy, N. B. Alamdari, J. S. Hamilton, J. C. Scott, *Langmuir* **2005**, *21*, 5034–5039.

[21] I. Protasova, S. Heißler, N. Jung, S. Bräse, *Chem. Eur. J.* **2017**, *23*, 8703–8711.

[22] M. Hesse, H. Meier, B. Zeeh, S. Bienz, L. Bigler, T. Fox, *Spektroskopische Methoden in der organischen Chemie*, Georg Thieme Verlag, Stuttgart, **2016**.

[23] J. Langer, D. Jimenez de Aberasturi, J. Aizpurua, R. A. Alvarez-Puebla, B. Auguié, J. J. Baumberg, G. C. Bazan, S. E. J. Bell, A. Boisen, A. G. Brolo, J. Choo, D. Cialla-May, V. Deckert, L. Fabris, K. Faulds, F. J. García de Abajo, R. Goodacre, D. Graham, A. J. Haes, C. L. Haynes, C. Huck, T. Itoh, M. Käll, J. Kneipp, N. A. Kotov, H. Kuang, E. C. Le Ru, H. K. Lee, J.-F. Li, X. Y. Ling, S. A. Maier, T. Mayerhöfer, M. Moskovits, K. Murakoshi, J.-M. Nam, S. Nie, Y. Ozaki, I. Pastoriza-Santos, J. Perez-Juste, J. Popp, A. Pucci, S. Reich, B. Ren, G. C. Schatz, T. Shegai, S. Schlücker, L.-L. Tay, K. G. Thomas, Z.-Q. Tian, R. P. Van Duyne, T. Vo-Dinh, Y. Wang, K. A. Willets, C. Xu, H. Xu, Y. Xu, Y. S. Yamamoto, B. Zhao, L. M. Liz-Marzán, *ACS Nano* **2020**, *14*, 28–117.

[24] W. Yue, Z. Wang, Y. Yang, L. Chen, A. Syed, K. Wong, X. Wang, *J. Micromech. Microeng.* **2012**, *22*, 125007.

[25] P. Mosier-Boss, *Nanomaterials* **2017**, *7*, 142.

[26] D. Cialla, A. März, R. Böhme, F. Theil, K. Weber, M. Schmitt, J. Popp, *Anal. Bioanal. Chem.* **2012**, *403*, 27–54.

[27] G. Kolhatkar, J. Plathier, A. Ruediger, *J. Mater. Chem. C* **2018**, *6*, 1307–1319.

[28] P. Verma, *Chem. Rev.* **2017**, *117*, 6447–6466.

[29] S. Schlücker, *Angew. Chem. Int. Ed.* **2014**, *53*, 4756–4795; *Angew. Chem.* **2014**, *126*, 4852–4894.

[30] S. E. J. Bell, G. Charron, E. Cortés, J. Kneipp, M. L. Chapelle, J. Langer, M. Procházka, V. Tran, S. Schlücker, *Angew. Chem. Int. Ed.* **2020**, *59*, 5454–5462; *Angew. Chem.* **2020**, *132*, 5496–5505.

[31] M. Gellner, S. Niebling, H. Y. Kuchelmeister, C. Schmuck, S. Schlücker, *Chem. Commun.* **2011**, *47*, 12762–12764.

[32] Y. He, C. Song, L. Que, *Microsyst. Technol.* **2019**, *25*, 4349–4356.

[33] D. Cialla, U. Hübner, H. Schneidewind, R. Möller, J. Popp, *ChemPhysChem* **2008**, *9*, 758–762.

[34] A. E. Cetin, D. Etezadi, B. C. Galarreta, M. P. Busson, Y. Eksioglu, H. Altug, *ACS Photonics* **2015**, *2*, 1167–1174.

[35] Y. Zhang, Y. Hu, G. Li, R. Zhang, *Microchim. Acta* **2019**, *186*, 477.

[36] J.-A. Huang, Y.-L. Zhang, H. Ding, H.-B. Sun, *Adv. Opt. Mater.* **2015**, *3*, 618–633.

[37] N. K. Devaraj, J. P. Collman, *QSAR Comb. Sci.* **2007**, *26*, 1253–1260.

[38] J. K. Lee, Y. S. Chi, I. S. Choi, *Langmuir* **2004**, *20*, 3844–3847.

[39] E. C. Le Ru, E. Blackie, M. Meyer, P. G. Etchegoin, *J. Phys. Chem. C* **2007**, *111*, 13794–13803.

[40] X.-M. Lin, Y. Cui, Y.-H. Xu, B. Ren, Z.-Q. Tian, *Anal. Bioanal. Chem.* **2009**, *394*, 1729–1745.

[41] Y. Ling, W. C. Xie, G. K. Liu, R. W. Yan, D. Y. Wu, J. Tang, *Sci. Rep.* **2016**, *6*, 31981.

[42] D. Lin-Vien, N. B. Colthup, W. G. Fateley, J. G. Grasselli, *The Handbook of Infrared and Raman Characteristic Frequencies of Organic Molecules*, Academic Press, Boston, **1991**.

[43] M. Tireli, S. Maračić, S. Lukin, M. J. Kulcsár, D. Žilić, M. Cetina, I. Halasz, S. Raić-Malić, K. Užarević, *Beilstein J. Org. Chem.* **2017**, *13*, 2352–2363.

[44] K. Gordon, S. Balasubramanian, *J. Chem. Technol. Biotechnol.* **1999**, *74*, 835–851.